



## Article

# High-Throughput Live and Fixed Cell Imaging Method to Screen Matrigel-Embedded Organoids

Susanne Ramm <sup>1,2,\*</sup> , Robert Vary <sup>1</sup>, Twishi Gulati <sup>1,2</sup>, Jennii Luu <sup>1</sup>, Karla J. Cowley <sup>1</sup>, Michael S. Janes <sup>3</sup>, Nicholas Radio <sup>3</sup> and Kaylene J. Simpson <sup>1,2,4,\*</sup> 

<sup>1</sup> Victorian Centre for Functional Genomics, Peter MacCallum Cancer Centre, Melbourne, VIC 3000, Australia

<sup>2</sup> Sir Peter MacCallum Department of Oncology, University of Melbourne, Parkville, VIC 3010, Australia

<sup>3</sup> Thermo Fisher Scientific, Waltham, MA 02451, USA

<sup>4</sup> Department of Biochemistry and Pharmacology, University of Melbourne, Parkville, VIC 3010, Australia

\* Correspondence: susanne.ramm@petermac.org (S.R.); kaylene.simpson@petermac.org (K.J.S.)

**Abstract:** Technical advances in microscopy and automation have enabled image-based phenotypic screening of spheroids and organoids to become increasingly high throughput and high content at the same time. In particular, matrix-embedded 3D structures can recapitulate many aspects of parent (e.g., patient) tissues. Live-cell imaging of growing structures allows tremendous insight into population heterogeneity during drug treatment. However, screening for targeted markers and more detailed morphological analyses typically require fixation of 3D structures, and standard formaldehyde (FA) incubation conditions can dissolve collagen-based extracellular matrices such as Matrigel. The dislocation and clumping of the spheroids make image-based segmentation very difficult and the tracking of structures from the live cell stage to their fixed cell location virtually impossible. In this method, we present a fixation and staining protocol that is gentle enough to maintain 3D structures exactly in their live-cell location and does not alter their morphology. This opens up analytical strategies that connect the spheroid's growth kinetics and heterogeneity of treatment responses with the more targeted fixed cell stains. Furthermore, we optimized the automated seeding and imaging of spheroids so that screening and phenotypic characterization can be performed in high-throughput at either low or high magnification and yield the same result, independent of the microscope used.

**Keywords:** high-throughput screening; organoids; spheroids; high-content imaging; Matrigel; fixation; auto-fluorescence; cell tracking; phenotypic clustering; 3D



**Citation:** Ramm, S.; Vary, R.; Gulati, T.; Luu, J.; Cowley, K.J.; Janes, M.S.; Radio, N.; Simpson, K.J. High-Throughput Live and Fixed Cell Imaging Method to Screen Matrigel-Embedded Organoids. *Organoids* **2023**, *2*, 1–19. <https://doi.org/10.3390/organoids2010001>

Academic Editors: Elizabeth Vincan, Tony Burgess, Nick Barker and Joseph Torresi

Received: 15 October 2022  
Revised: 23 November 2022  
Accepted: 17 December 2022  
Published: 24 December 2022



**Copyright:** © 2022 by the authors. Licensee MDPI, Basel, Switzerland. This article is an open access article distributed under the terms and conditions of the Creative Commons Attribution (CC BY) license (<https://creativecommons.org/licenses/by/4.0/>).

## 1. Introduction

Over the last 20 years, the technological advances in automated microscopy have allowed researchers to take image-based high-content screens from 2D [1] into 3D cultures with an ever increasing number of conditions and extracted content [2]. 3D models have been found to be more in vivo-like regarding their gene expression and cell behavior [3,4], and more predictive of both in vivo toxicity and therapeutic efficacy [5,6]. Trying to fulfil the promise of providing an in vivo-relevant test platform, researchers have invested heavily in increasing the speed and accuracy with which 3D models can be screened [7].

Imaging cultures in 96- or 384-well format, embedded in an extracellular matrix (ECM) such as Matrigel, allows for the extraction of additional information on population heterogeneity and changes to the composition of the population over time and during treatment [8]. Using brightfield or fluorescence imaging with live specimens is ideal, fast, and low cost, but adopting more targeted staining protocols for cell morphology panels with antibodies or with small molecule fluorescent probes such as Cell Painting [9] requires fixation and permeabilization of the spheroids. Yet, fixation of 3D structures embedded in Matrigel with standard formaldehyde (FA) methods dissolves the ECM. This generates three main problems for image-based phenotyping:

- (i) It changes the relative position of organoids in the well, which makes tracking of individual structures impossible.
- (ii) It can change the original morphology of organoids because of the loss of the supporting matrix, especially larger structures or cystic organoids.
- (iii) Organoids are likely to form clumps that are very hard to segment during image analysis, which makes single organoid analyses almost impossible.

Different groups have devised different strategies to address these challenges. One solution includes fixing the organoids with formaldehyde and subsequent embedding into paraffin [10]. However, this method is very laborious, hard to automate, and so far, is not suitable for high-throughput screening. Another approach is to grow organoids in U-bottom plates without any scaffold [11]. These assays can be run in high-throughput; however, they provide neither inbuilt replicates nor information on population heterogeneity within each well as with matrix-based embedding. More importantly, the 3D objects grown in U-bottom plates have no supporting ECM scaffold, which has been widely recognized as a critical component in various organoid cultures and is thought to be a requirement for more physiologically and translationally relevant organoid models [12]. Finally, much effort is invested into the development of alternatives to Matrigel. A big advantage of these hydrogel-based matrices is that, compared to Matrigel, they tend to be less sensitive to dissolution during FA fixation and the location and shape of the organoids is better maintained. However, they require extensive optimization for each organoid culture and are still compared to Matrigel as the “gold standard” [10,13].

We realized that bringing commonly used high-content imaging methods from 2D cells into the 3D organoid world would require a FA-independent method for fixing and staining Matrigel-embedded heterogeneous structures directly in the well. Therefore, we developed a gentle fixation method that maintains the original morphology and position of each organoid in a 384-well plate and is fully automated. This way, the data generated on each live-cell organoid (e.g., growth kinetics) can be related to the more specific, targeted fixed cell stains, querying the underlying biology of the heterogeneous response. This method will allow researchers to position their assays of interest anywhere along our automated, flexible workflow (see graphical abstract), irrespective of scale. The retention of organoid location and morphology, independent of magnification or microscope, permits a true integration of live and fixed cell high-throughput imaging methods, which reduces the required amount of precious patient cells and expensive Matrigel.

## 2. Materials and Methods

### 2.1. Cell Culture and Spheroid Preparation

The MCF7 breast cancer cell line was purchased from American Type Culture Collection (ATCC) and grown in Gibco™ DMEM (Thermo Fisher Scientific, Waltham, MA, USA) supplemented with 10% HyClone Fetal Bovine Serum (GE Healthcare, Chicago, IL, USA). The MR49F prostate cancer cell line and two patient-derived prostate cancer organoids 201.1A-Cx (201DURA; representing androgen receptor-positive, castrate-resistant prostate cancer) and 287R (representing androgen receptor-positive, castrate-sensitive prostate cancer) were obtained from Gail Risbridger and Mitchell Lawrence at Monash University (Clayton, Victoria, Australia). Both patient-derived prostate cancer organoids have previously been extensively characterized [14].

A 10 µL base layer of 80% Matrigel (growth factor-reduced, phenol-red free, IdEV-free, 9.3 mg/mL stock concentration; lot number 1237002; Corning, NY, USA) was robotically dispensed in each well of black-walled, clear bottom 384-well Corning plates (cat # 3764) and allowed to set for 10 min at 37 °C/5% CO<sub>2</sub>.

MCF7 breast cancer cells were robotically seeded in 10 µL (containing 2000 cells) of a 2% Matrigel suspension on top of the solidified base layer using a Janus G3 liquid handling robot with a cooled stage (PerkinElmer, Waltham, MA, USA), as described previously [8]. The Matrigel was allowed to set for 15–20 min at 37 °C/5% CO<sub>2</sub> followed by the addition of 25 µL media using an EL406 liquid handling workstation (BioTek Instruments, Winooski,

VT, USA). MR49F prostate cancer cells and patient-derived prostate cancer organoids (201DURA and 287R) were seeded the exact same way but in 10  $\mu$ L (containing 2000 cells) of a 50% Matrigel suspension on top of the solidified base layer. Cells were subsequently cultured in a LiCONiCs STX220 incubator (LiCONiC, Lichtenstein, Germany) at 37 °C/5% CO<sub>2</sub> for the duration of the experiment.

On day 4 of culture, 20  $\mu$ L media was aspirated using the EL406 liquid handling workstation, leaving 5  $\mu$ L media as dead volume and 20  $\mu$ L Matrigel in the well. Then, 20  $\mu$ L fresh complete media was added to the spheroids, making the final volume in the well to 45  $\mu$ L.

This layering of 25  $\mu$ L media on top of 10  $\mu$ L diluted Matrigel (between 2 to 50% depending on cell type) on top of 10  $\mu$ L base layer of 80% Matrigel allowed for easy automation due to a clear separation between Matrigel and liquid media. All liquid handling steps, ranging from seeding, media changes, drug treatments, to fixing and staining, required no manual pipetting, thereby reducing errors and increasing reproducibility and throughput.

### 2.2. Live-Cell Image Acquisition

Live spheroids were imaged via brightfield microscopy using the Cytation C10 Cell Imaging Multi-Mode Reader (BioTek) at 4 $\times$  magnification (one field/well, maximum projection of a stack of three z-heights 100  $\mu$ m apart). Our layered seeding protocol ensures that the embedded organoids are always in a defined z-height range in the plate. These daily images were used to monitor growth, identify the ideal time point for the beginning (day 4) and the end (day 7) of drug treatment, and perform single organoid tracking.

### 2.3. Fixing and Quenching

We performed a series of optimizations to fix cells embedded in Matrigel (Table 1) using 0.1–1% glutaraldehyde (ProSciTech, Townsville, Queensland, Australia) or a combination of 2–4% FA (sold as PFA; ProSciTech), diluted in PBS, with or without a pre-treatment with 18% sucrose (Sigma-Aldrich, St. Louis, MO, USA). All incubations were performed at room temperature.

**Table 1.** Conditions evaluated to fix cells embedded in Matrigel.

Pre-Treatment	Fixative	Concentration (v/v%)	Incubation Time (Minutes)
None	FA diluted in PBS	2, 4	10
Sucrose	FA diluted in PBS	2, 4	1, 3, 5, 10
None	Glutaraldehyde diluted in PBS	0.1, 0.3, 0.5, 1	1, 3, 5, 10
None	Glutaraldehyde diluted in PBS	0.4	10

To quench background auto-fluorescence, we evaluated post-fixation treatment with sodium borohydride (Sigma-Aldrich) across a range of concentrations (%), incubation times, and temperatures (Table 2).

**Table 2.** Quenching conditions in Matrigel-embedded fixed cells using sodium borohydride.

Concentration (%) of Sodium Borohydride	Incubation Time	Incubation Temp.
0.5	20 min	RT
0.5	35 min	RT
1, 3, 5	60 min	RT
1, 1.5, 2	18 h	4 °C
0.7, 0.8, 0.9	18 h	4 °C
0.05, 0.2, 0.5	1, 4 h	4 °C

All sodium borohydride optimization conditions were tested after fixing the spheroids in 0.4% glutaraldehyde for 10 min at room temperature.

Sodium borohydride powder (Sigma-Aldrich, Cat. 452882-25G) was dissolved in ultrapure water to a stock concentration of 1% (1g/100 mL). For the lower concentrations, the stock was further diluted in ultrapure water.

Our optimized protocol consisted of fixation in 25  $\mu$ L 0.4% glutaraldehyde for 10 min at room temperature, followed by two washes with 50  $\mu$ L PBS, quenching with 25  $\mu$ L 0.2% sodium borohydride for 1 h at 4  $^{\circ}$ C, and washing three times with PBS. All liquid handling steps were performed using the EL406 liquid handling workstation. For washing steps and change of reagents in the wells, we aspirated at a distance from the Matrigel that left 6  $\mu$ L dead volume in the well to protect the integrity of the matrix. The plates with PBS can be sealed and stored at 4  $^{\circ}$ C until staining and imaging.

#### 2.4. Multiplex Staining of Spheroids to Image Fixed Cells

Our multiplex staining strategy requires both live and fixed staining conditions (Table 3). On day 7 after seeding, live spheroids were incubated in media containing Invitrogen™ MitoTracker™ Deep Red dye (Thermo Fisher Scientific). This particular dye needs to be added to live cells but is stable throughout the fixing process and was therefore chosen to be part of our fixed cell staining panel. Spheroids were then fixed at RT, quenched, washed with PBS, and stained with DAPI (4',6-diamidino-2-phenylindole; Sigma-Aldrich), Invitrogen™ Wheat Germ Agglutinin, Alexa Fluor™ 594 Conjugate (WGA; Thermo Fisher Scientific), and Rhodamine Phalloidin (Biotium, Fremont, CA, USA) in the presence of 0.1% Triton X-100 (Sigma-Aldrich) in PBS. All liquid handling steps were performed using the EL406 liquid handling workstation. The stained plates with 50  $\mu$ L PBS were sealed using non-transparent foil and stored at 4  $^{\circ}$ C until imaging.

**Table 3.** Multiplexed staining panel.

Target	Reagents	Catalog Number	Stock	Final Dilution	Diluent	Incubation Time and Temp.
Mito-chondria	MitoTracker Deep Red dye	M22426	1 mM	1:500	Media	2 h at 37 $^{\circ}$ C in incubator
Nuclei	DAPI	D9542	5 mg/mL	1:1000	50 mM Tris pH 7.6	2 h at RT
Golgi	Alexa Fluor 594-WGA	W11262	1 mg/mL	1: 00	50 mM Tris pH 7.6	2 h at RT
F-Actin cyto-skeleton	Rhodamine Phalloidin	00027	200 Units/mL (~6.6 $\mu$ M)	1: 50	50 mM Tris pH 7.6	2 h at RT

#### 2.5. Fixed-Cell Image Acquisition

Fixed and stained spheroids were imaged at 20 $\times$  magnification (four fields/well, stack of five z-heights 8  $\mu$ m apart) using a Thermo Scientific™ CellInsight CX7 LZR High-Content Screening (HCS) Platform (Thermo Fisher Scientific). The following channels were assigned to capture the staining panel: (1) DAPI (405 nm, widefield for autofocus), (2) DAPI (405 nm, confocal), (3) Rhodamine Phalloidin (488 nm, confocal), (4) Alexa Fluor 594-WGA (561 nm confocal), (5) MitoTracker Deep Red dye (MTDR, 647 nm, confocal), (6) Brightfield (White-BF). Autofocus was performed in every field in the DAPI widefield channel with 4  $\times$  4 binning. Confocal images were captured with a pin hole size of 70  $\mu$ m diameter and 2  $\times$  2 binning.

#### 2.6. Compound Screen

A small compound library comprising 56 compounds, selected to represent 13 different mechanisms of action (e.g., MEK inhibition, microtubule disruption, cell cycle inhibition), was screened over a five-point dose range (10, 5, 3, 1, 0.1  $\mu$ M). Compounds were sourced

from Compounds Australia (Griffith University, Nathan, Queensland, Australia) and provided in assay-ready lyophilized form. Compounds were resuspended in complete culture media. On day 4 post-seeding, using the Janus G3 robot, the hydrated compounds were transferred to two replicate experimental plates with 5  $\mu$ L added to 45  $\mu$ L media/Matrigel.

Three positive controls (staurosporine, mitomycin C, doxorubicin), one vehicle control (0.2% DMSO), and one negative control (media only) were included in the outer wells. Positive control compounds were added using a D300e digital dispenser (Tecan, Männedorf, Switzerland) to four replicates per drug with final concentrations of 10, 1, and 0.1  $\mu$ M. The vehicle control (0.2% DMSO) was added to 48 wells and media alone to 20 wells.

Cells were incubated 37 °C/5% CO<sub>2</sub> for 72 h prior to fixing and staining.

### 2.7. Image Analysis

All image analyses were performed using CellProfiler software (Broad Institute of MIT and Harvard, Cambridge, MA, USA, version 4.1.3), with all analysis pipelines fully customized.

For images captured at 4 $\times$ , spheroid segmentation into primary objects was performed based on the Brightfield channel. We added a filter step to exclude objects touching the border of the field and debris (area < 100 px<sup>2</sup>) from further analysis. For subsequent quantification of spheroid morphology, including area, radius, and eccentricity, as well as texture and intensity features, we used well-level averages, except for single-spheroid analyses that were used for tracking of organoids over time.

For z-stack images captured at 20 $\times$ , spheroid segmentation into primary objects was performed based on each z-slice individually on the DAPI channel. Here, objects touching the border of the field were not excluded but were filtered out based on size (area < 1000 px<sup>2</sup>) to remove debris and based on very low overall DAPI intensity (Max-DAPI\_Intensity < 0.03) to remove spheroids located on very different focal planes. Per 20 $\times$  field, we identified between zero and nine spheroids with an average of four across a 384-well plate. In a second step, we identified nuclei in each spheroid based on the DAPI channel as a second population and defined the cell boundaries based on Phalloidin staining. For subsequent quantification of spheroid and single cell morphology, including area, radius, and eccentricity, as well as texture and intensity features, we extracted image/field-level medians and standard deviations of each z-slice separately (total of 4199 imaging features across five channels and two object populations).

### 2.8. Data Analysis

All data derived from image feature extraction was analyzed in the RStudio/posit statistical environment (v1.2.1335; Boston, MA, USA) using the tidyverse package (v1.3.1). To ensure that all features were the same scale for phenotypic profiles, we calculated Z-scores as described previously [8]. Heat maps were generated based on spheroid solidity z-scores at day 3, 4, 5, and 7 (before and after fixing) using the dplyr (v1.0.8) and platetools (v0.1.2) packages.

In the first step, all fields that did not contain any objects were excluded. Next, we aggregated the data from individual fields and z-slices into per-well data and revised the 4199 features down to a “clean” set of 4119 based on the following criteria:

- (i) inactive features with low/no variance (=69 features removed).
- (ii) features containing NA, NaN, or Inf (=11 features removed).

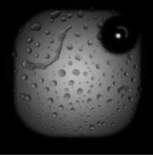
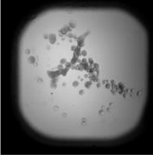

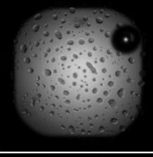
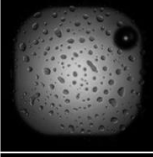
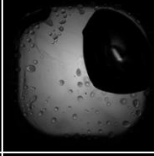

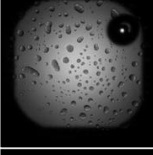
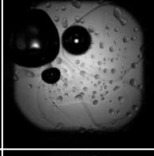
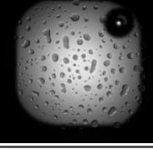
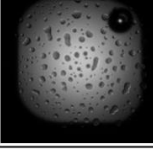
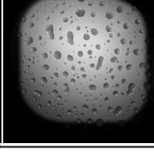
To select active compounds, we excluded negative (vehicle, media) and positive controls (mitomycin C, staurosporine, doxorubicin) and calculated Mahalanobis distances (M-distance) and multidimensional perturbation values (mp-value) for all library compounds based on their clean feature vectors. We used published R functions [15] that we slightly modified for our purpose ([https://rdrr.io/github/lucyleeow/CellProfileR/src/R/calc\\_mp.R](https://rdrr.io/github/lucyleeow/CellProfileR/src/R/calc_mp.R); accessed 19 December 2022). The cut-off for active compounds was set very relaxed at a M-distance of 1, which left 48 compounds for clustering.

Next, we performed unsupervised feature reduction. Redundant features with high feature correlation (based on Pearson correlation coefficient  $< 0.55$  using the caret package (v6.0-88; developed by Max Kuhn, Department of Statistics, University of Wisconsin-Madison, Madison, WI, USA, 2020; accessed 19 December 2022)) were removed (=3969), leaving a final set of 150 features. Hierarchical clustering was performed on concatenated final feature vectors that consisted of all five concentrations of each drug. We used the factoextra library (v1.0.7; developed by Abderrahim Kassambara, Department of Statistics, University of Wisconsin-Madison, Madison, WI, USA, 2020; accessed 19 December 2022) with euclidean distance metric and average linkage to generate dendrograms. Graphs of phenotypic profiles were generated using the ggplot2 package (v3.3.5; developed by Hadley Wickham, Department of Statistics, Rice University, Houston, TX, USA, 2016; accessed 19 December 2022).

### 3. Results

#### 3.1. Optimisation of Fixation and Quenching

FA fixation of spheroids dissolved our Matrigel (stock protein content 9.3 mg/mL) to varying degrees at all concentrations tested (4% down to 0.01%) and occurred irrespective of the incubation length and temperature (RT, 4 °C) (Supplementary Figure S1). The loss of the supporting matrix changed the position of all spheroids in the well and created large aggregates of spheroids towards the center of the well (Figure 1, Panel 1). Segmentation of single spheroids using our image analysis pipelines and more importantly, tracking of fixed spheroids back to their location during the growth period was not possible after FA fixation.

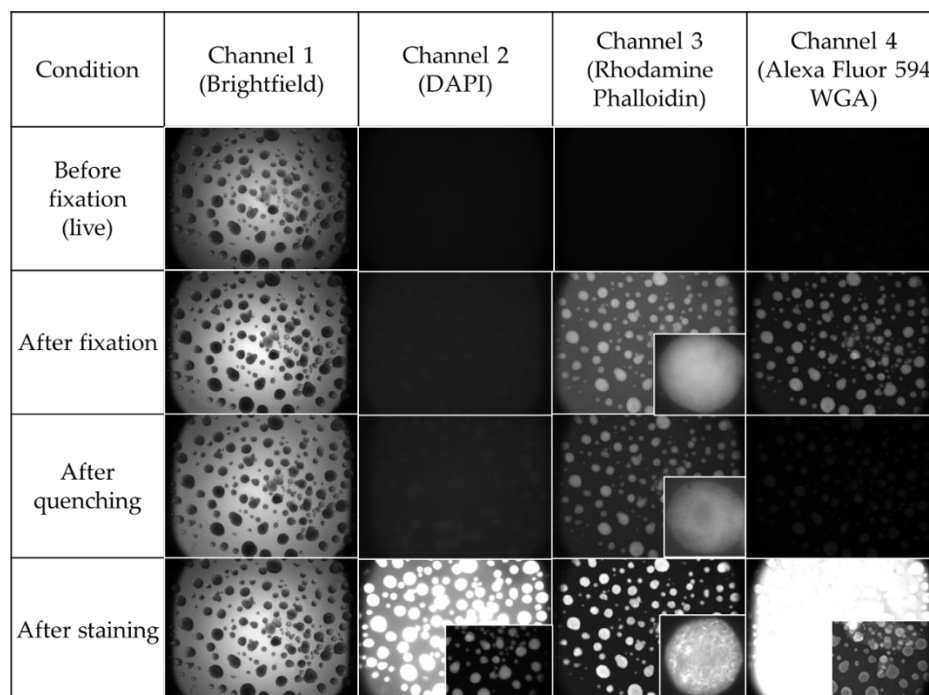
	Description	Before fixation (live)	After fixation	After quenching
1	FA (4%), 10min RT <i>Dissolved the matrix</i>			
2	Glutaraldehyde (0.4%) 1% NaBH4 at RT for 1h <i>Loss of matrix and organoids</i>			
3	Glutaraldehyde (0.4%) 1% NaBH4 at 4 °C for 1h <i>Major damage to gel surface</i>			
4	Glutaraldehyde (0.4%) 0.2% NaBH4 at 4 °C for 1h <i>Final method</i>			

**Figure 1.** Optimization of fixing and quenching protocols with example Brightfield images at 4×.

In a first optimization step, we changed formaldehyde to glutaraldehyde. At 0.3 to 1%, the new fixative agent maintained the position of spheroids in the matrix. The ability to fix objects in Matrigel was lost at very low glutaraldehyde concentrations of 0.1%. Optimal fixation was achieved using 0.4% glutaraldehyde for 10 min at RT (Figure 1, Panel 2).

However, fixation with glutaraldehyde created free aldehyde groups, resulting in minor auto-fluorescence in the DAPI channel (405 nm) and stronger auto-fluorescence

at 488 (green), 561 (red), and 647 nm (deep red) (Figure 2), which was not conducive with staining and imaging strategies. We used sodium borohydride to reduce the aldehyde groups generated during the fixation process to hydroxyl groups [16] and thereby quenched the auto-fluorescence. However, incubation with 1% sodium borohydride at RT released hydrogen gas upon contact with water (<https://www.sciencedirect.com/topics/pharmacology-toxicology-and-pharmaceutical-science/sodium-borohydride>; accessed 19 December 2022) and generated bubbles that were trapped in the Matrigel. This resulted in loss of Matrigel and spheroids in the treated wells (Figure 1, Panel 2). Changes to the incubation temperature from RT to 4 °C reduced the loss of matrix but the gas bubbles caused shifting of spheroids in the Matrigel and some got trapped in the matrix, which made an imaging strategy impossible (Figure 1, Panel 3). Next, we reduced the concentration of sodium borohydride to 0.2% and below (Figure 1, Panel 4). We concluded near perfect retention of spheroids in their original position was achieved using 0.2% sodium borohydride for 1 h at 4 °C (Figure 1, Panel 4 and Figure 2). The quenching with 0.2% worked very well in the red channel (Figure 2) and similarly in the far-red channel (images not shown). However, it only had a minor quenching effect in the green channel (reduction of intensity by approximately 30 to 40%). To remove the auto-fluorescence by more than 75%, quenching with at least 1% sodium borohydride was necessary but that induced major damage to the Matrigel and did not retain the location of spheroids. Therefore, remaining minor auto-fluorescence in the 488 nm channel was accepted in our final method. We mitigated the remaining auto-fluorescence by use of the green channel for either very bright markers or dyes that label structures easily distinguishable from the non-specific background, such as F-actin (Figure 2).



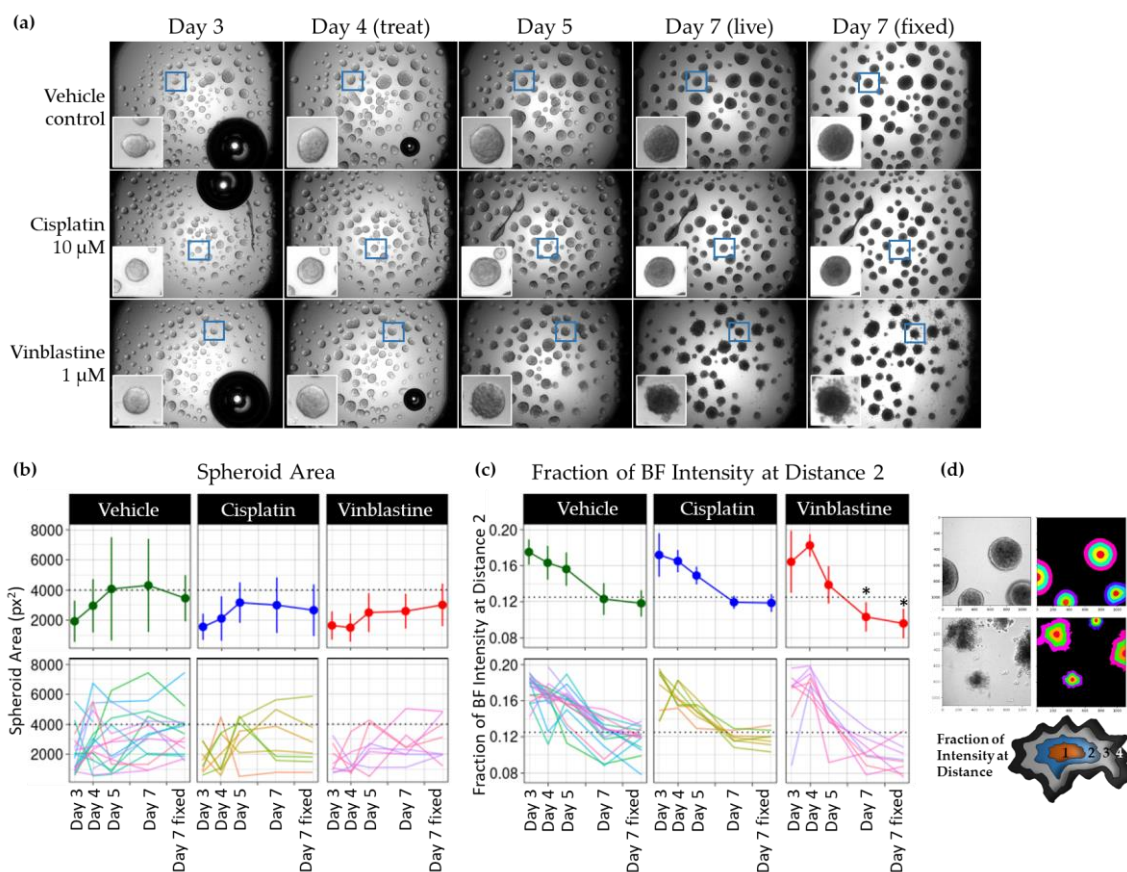
**Figure 2.** Induction of auto-fluorescence glutaraldehyde fixation and decrease of auto-fluorescence using sodium borohydride quenching at 0.2%. All large images (2.5×, Cytation 5) were taken with the same exposure time in each respective channel. DAPI and Alexa Fluor 594-WGA staining are over-saturated at high exposure times and small images show organoids at lower exposure time. Small images in channel 3 (20×, CellInsight CX7 LZR platform) show Rhodamine Phalloidin staining of F-actin structures that supersede the background fluorescence.

This fixing, quenching, and staining protocol was optimized using MCF7 breast cancer spheroids in 2% Matrigel. However, we successfully used the exact same protocol in

spheroids from other cell lines (MR49F prostate cancer) and patient-derived prostate cancer organoids, grown in 50% Matrigel, without having to change any part of the method.

### 3.2. Optimized Method Allows Single Spheroid Tracking over Time and Post-Fixation

Monitoring of organoids and spheroids over time using live-cell brightfield imaging offers a range of analytical advantages and strategies (Figure 3a).



**Figure 3.** (a) Time course of brightfield images across live and fixed cells (2.5×, Cytation 5). Individual organoid (blue square) is shown in higher magnification over time. (b) Area plotted as average (circles) and standard deviation (error bars) of at least 7 individual spheroids (top panel) and as single object traces (bottom panel). Reduced area growth in spheroids treated with cisplatin (10 μM) and vinblastine (1 μM) compared to vehicle controls (0.2% DMSO). (c) Vinblastine (1 μM) significantly decreases the Fraction of brightfield (BF) intensity at Distance 2 compared to vehicle control at the same time point, corresponding to a darkening of the spheroid center at day 7. (\*  $p < 0.03$ , ANOVA, Šidák's multiple comparisons test) (d) Visual representation of Radial Distribution (Intensity Fraction at four Distances, labelled 1, 2, 3, 4 radiating from the center) in vehicle controls (top) and vinblastine (5 μM) treated wells (bottom), a frequently used spheroid shape descriptor.

Firstly, at the initial stages of a 3D project, cultures were optimized for screening purposes by generating growth curves and thereby determining the optimal time points for the start and the end of drug treatments during the exponential growth phase of the culture. In MCF7 spheroids, a doubling of the area occurred between day 3 and 5, before the growth plateaued around day 7 (Figure 3b, top panel). Two example drug treatments with different mechanisms of action (10 μM cisplatin and 1 μM vinblastine) inhibited the growth compared to control already at day 5, 1 day after the start of the 3-day treatment.

Secondly, single organoid segmentation allowed tracking of individual spheroids over time (Figure 3b, bottom panel). This data can be used to gain insight into population



heterogeneity in each well and monitor for example if organoids that start out smaller or grow slower respond differently to drug treatment than larger or faster growing structures.

Thirdly, brightfield (BF) images allow for the extraction of shape, intensity, and texture features that can serve as a readout for certain toxic responses. The Fraction at Distance (FractAtD) feature describes the mean intensity in the BF image in one of four rings drawn around the center of the spheroid (Figure 3d). Vinblastine induced a significant decrease (darkening) in Distance 2 compared to vehicle-treated controls (Figure 3c, top panel). The traces from individual tracked spheroids show that the optimized fixation and quenching process was so gentle that the internal spheroid composition, based on the FractAtD feature, was not significantly altered compared to the images taken from live cells (Figure 3c, bottom panel, Day 7 vs. Day 7 fixed).

### 3.3. Optimisation of Screening Conditions to Allow for High Throughput

The three-dimensionality of the objects and embedding in a matrix introduces additional challenges into the screening of organoids and spheroids in high-throughput. Four main circumstances can cause drastic increase in imaging time per plate and therefore prevent higher throughput outcomes:

- (i) The 3D objects are distributed throughout the whole z-height of a large Matrigel dome and require lengthy autofocus in each well or even each individual field.
- (ii) The method is very specific to a certain cell type and cannot be generalized to a large range of cell types and Matrigel concentrations.
- (iii) After finding the first focal plane, the assay requires a large z-stack in each field.
- (iv) The distribution of the 3D objects in the well is not even or too sparse, which requires dozens of fields when imaging at higher magnifications—because many fields will be empty.

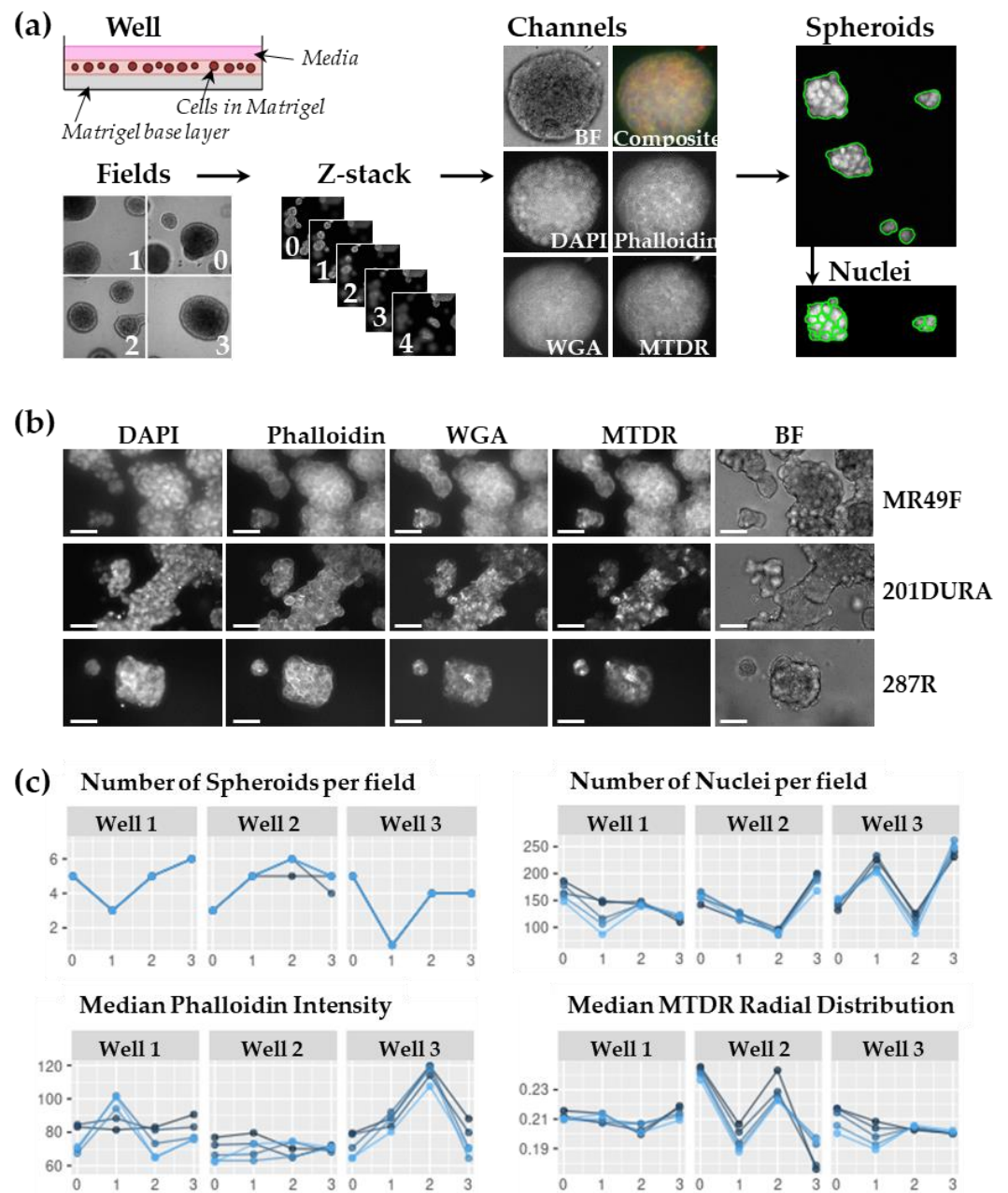
Addressing the first point, our automated seeding protocol, depositing 10  $\mu$ L of Matrigel-cell suspension, consistently resulted in an even distribution of the spheroids across the 384 wells (Figures 1–3). This allowed us to set a fixed focal height for the whole plate when screening at 2.5 $\times$  (Cytation 5) or 4 $\times$  (Cytation C10), rather than autofocusing in each well. The fixed focal height depended on the plate type used and it cut the imaging time per 384-well plate down to 20 min with 3 z-heights (80  $\mu$ m apart; for low seeding densities or very high Matrigel concentrations), 14 min with 2 z-heights (80  $\mu$ m apart; our standard for MCF7 screening), or just 7 min with a single imaged z-plane (sufficient for optimizations).

In Figure 4b we apply our fixing, quenching, staining, and imaging method to a different cell line (MR49F prostate cancer cells) and two different patient-derived prostate cancer organoids (201DURA, 287R). Irrespective of the difference in their size, shape, and Matrigel concentration, our workflow could be applied to all spheroids and organoids without having to be altered or further optimized. However, due to their different shape, the downstream image analysis pipelines might have to be adjusted to accommodate different segmentation thresholds.

Turning to the third point, after fixing and staining, we imaged our 3D plates at 20 $\times$  confocal (CellInsight CX7 LZR platform) to extract single organoid and single nuclei data across five channels (Figure 4a, here BF, DAPI, Rhodamine Phalloidin, Alexa Fluor 594-WGA, and MitoTracker Deep Red (MTDR)). An ideal imaging method would capture the highest possible variance present in the 3D objects with the lowest possible number of images that need to be taken.

We acquired images in four fields per well at 20 $\times$  magnification of six wells, treated with a vehicle control (0.2% DMSO). After autofocusing in each field, we took five z-stack images (8  $\mu$ m apart). The individual z-slices were analyzed and plotted separately (Figure 4c). A selection of imaging features from different channels for either whole spheroid or single nuclei-based measures showed that the majority of the variability in the data depended on the individual fields (0.5 to 50% with an average CV of 19%). The

coefficient of variation between the five z-slices only ranged between 0 and 20 % with an average of 5%.



**Figure 4.** (a) Schematic overview of image acquisition of spheroids grown in a diluted Matrigel layer on top of a high concentration Matrigel base layer. Four fields/wells (labelled 0, 1, 2, 3) captured on CX7 LZR (20 $\times$ ) across five z-slices (labelled 0, 1, 2, 3, 4) and across five channels. Segmentation for data extraction is based on both spheroids and single nuclei in each spheroid. (b) Representative images of untreated prostate cancer cells grown in Matrigel captured on CX7 LZR (20 $\times$ ) across five z-slices and across five channels: MR49F is a cell line; 201DURA and 287R are organoids from patient-derived prostate cancer xenograft models. (c) Selection of Nuclei- or Spheroid-based imaging features in three vehicle-treated control wells across all captured fields and z-slices. Different shades of blue of circles and lines correspond to results extracted from five z-heights.

The last of the four reasons that cause a drastic increase in imaging time at 20 $\times$  magnification is an uneven distribution of 3D objects. This can cause the majority of fields to be empty and requires the acquisition of a large number of fields per well. In a first step

of data clean up, all wells/fields/z-slices that did not contain any objects were excluded from our example 384-well compound screen plate. In total, thanks to our automated seeding protocol that ensures very even distribution of the spheroids, only 36 fields were without detectable spheroids, which corresponded to 2% of the fields of our 384-well plate (four fields per well). This rate of unusable fields was so low that we did not have to further address it in our analysis pipeline.

In summary, our optimized seeding and imaging protocols allowed us to screen 384-well plates at low magnifications in less than 15 min per plate (Cytation) and at high magnifications and both brightfield and four fluorescence channels (with minimal field numbers and only one z-height required) in only one hour (CellInsight CX7 LZR platform).

### 3.4. High-Content Screen with Optimized Fixing and Staining Method

#### 3.4.1. Results before and after Fixation and Across Imaging Platforms

We applied our optimized fixing, quenching, staining, and imaging protocols to perform a proof of principle high-content screen with a library of 56 compounds containing well-known mechanisms of action (MOA) (Supplementary Table S1). The drugs were screened at five concentrations (0.1, 1, 3, 5, and 10  $\mu$ M) and positive and negative controls were located around the outside wells of the plate (Figure 5a).

To confirm that the fixation and quenching process was gentle enough to preserve the live-cell imaging results (Figure 3c, bottom Panel, Day 7 vs. Day 7 fixed), we extracted average spheroid Solidity from each well at each live-cell time point and after fixation (Figure 5c). This imaging feature describes the proportion of the pixels in the convex hull that are also in the object, i.e.,  $\text{ObjectArea}/\text{ConvexHullArea}$  (Figure 5b). The Solidity feature can detect changes to the spheroid shape that correspond to the loss of roundness and integrity happening with drug-induced cell death.

Plotting of spheroid Solidity z-scores over the course of our drug screen, spanning live-cell brightfield imaging and fixed cell imaging ( $4\times$ ; Cytation C10), proved that drug-induced changes to spheroid shapes are well maintained and highly correlated irrespective of the fixation state (Figure 5d). Additionally, we identified the same drugs as toxic based on the Solidity feature, both in fixed cells at  $20\times$  (CellInsight CX7 LZR platform, four fields) and in  $4\times$  (Cytation C10, one field) images, indicating high versatility of this assay platform. However, the  $20\times$  acquisition demonstrated an increase in sensitivity to detect drug-induced changes in spheroid morphology at lower concentrations, therefore, we used this method for the more advanced analyses and clustering of imaging phenotypes.

#### 3.4.2. Unsupervised Feature Reduction

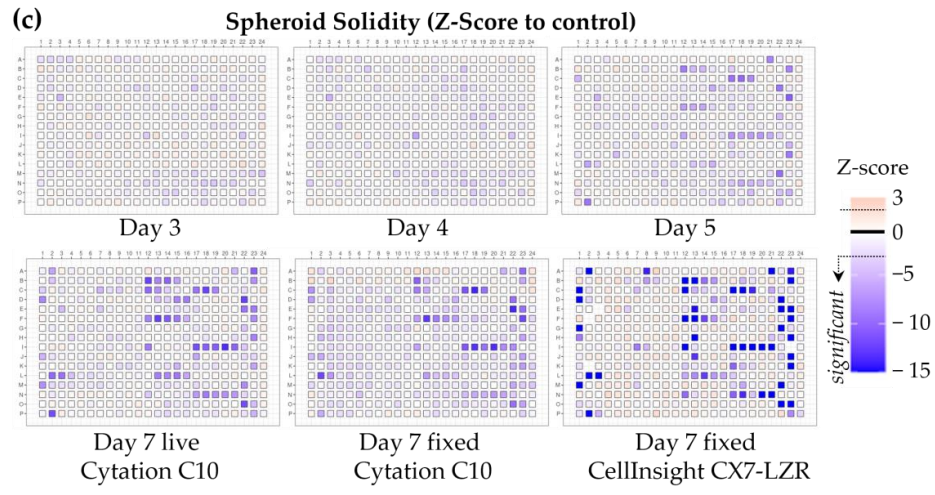
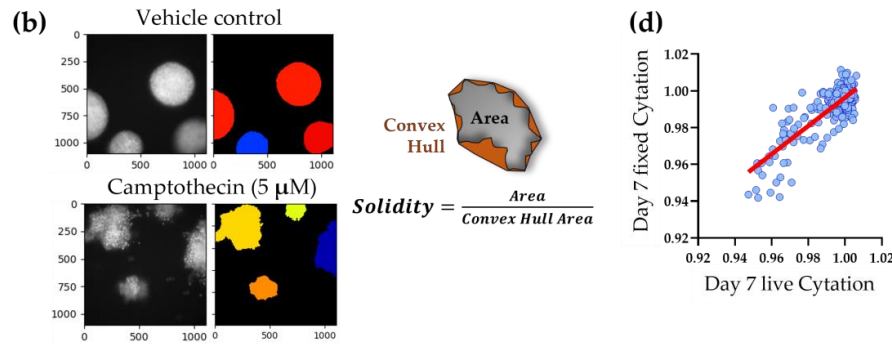
To prepare the extracted imaging features for clustering, we first performed unsupervised feature reduction. The final feature set consisted of 150 features in total, of which 66 features described the Median per well, 82 features described the Standard Deviation per well, and two features described Spheroids counts and Nuclei counts per well (see Supplementary Table S2). The distribution across different CellProfiler feature extraction algorithms was the following: 100 features described shape and morphology, 17 described intensity-based changes, 10 described Radial Distribution of intensity, 10 related to Texture, nine described Neighbours, and five features were Location based. The majority of the Area and Shape features (83) were from the family of Zernike shape calculations. These metrics of shape describe a binary object in a basis of Zernike polynomials, using the coefficients as features [17]. In our CellProfiler pipeline, Zernike polynomials from order 0 to order 9 were calculated, giving 30 measurements per Object (Spheroids, Nuclei) in both Median and Standard Deviation (120 in total). Since Zernike polynomials are orthogonal to each other, Zernike moments can represent properties of an image with no redundancy or overlap of information between the moments, which is why our unsupervised feature reduction method maintained such a large number of Zernike features in the final set.

**(a)**

	1	2	3	4	5	6	7	8	9	10	11	12	13	14	15	16	17	18	19	20	21	22	23	24	
A	1	10	0.2	0.2	0.2	0.2	0.2	0.2	0.2	0.2	0.2	0.2	0.2	0.2	0.2	0.2	0.2	0.2	0.2	0.2	0.2	1	0.2	10	0
B	0.2		Selumetinib					Dabrafenib						Nocodazole				Andrographolide				1	1	0	
C	10		PD184352					GW5074						Mitomycin C				Camptothecin				1	0.2	0	
D	10		Gefitinib					MLN2480						Docetaxel				Epirubicin				0.1	0	0	
E	0.2		PD98059					TAK-632						Cytarabine				Acadesin				10	0.1	0	
F	0		Vemurafenib					Voxtalisisib						Vinblastine				Phenformin				0.2	10	0	
G	1		Pimasertib					AZD8330						Cisplatin				Curcumin				10	0.1	0	
H	0.2		BIX 02188					Binimetinib						Altretamine				Chlorambucil				1	10	0	
I	1		BIX 02189					Sorafenib						Parthenolide				Colchicine				0.1	0.2	0	
J	0.1		PD318088					PLX7904						Anastrozole				Noscapine				1	10	0	
K	0.2		S8590885					Cobimetinib						Etoposide				Fluvastatin				0.1	0.1	0	
L	0.1		TAK-733					Palbociclib						Paclitaxel				Lovastatin				0.2	0.2	0	
M	10		Trametinib					Abemaciclib						Sirolimus				Mevastatin				1	0.1	0	
N	0.2		ZM 336372					Tacrolimus						Simvastatin				Triptolide				1	0.2	0	
O	1		AZ 628					Erlotinib						Eloxatin				Metformin				10	10	0	
P	0.1	0.1	0	0.2	0.2	0.2	0.2	0.2	0.2	0.2	0.2	0.2	0.2	0.2	0.2	0.2	0.2	0.2	0.2	0.2	0.2	0	0.1	0	

<b>positive controls</b> Doxorubicin, Staurosporin, Mitomycin C 0.1uM 1uM 10uM	<b>negative controls</b> DMSO (0.2%) Media	<b>library compounds</b> 0.1uM 1uM 3uM 5uM 10uM
---	--	--



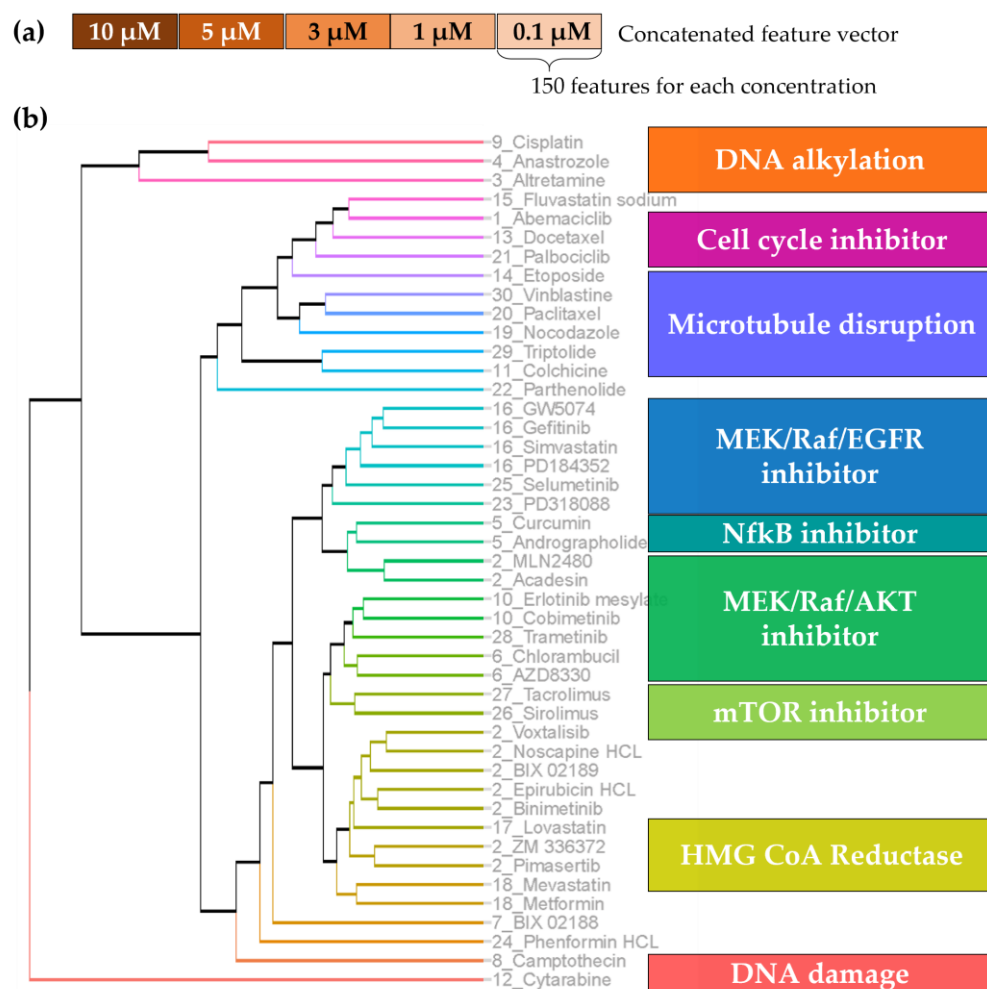
**Figure 5.** (a) Compound library plate (384 well plate coordinates from columns 1-24 and rows A-P) layout indicating location and concentration of vehicle and negative controls (0.2% DMSO, media), positive controls, and library drugs. (b) Visual representation and mathematical equation of Solidity, a frequently used spheroid shape descriptor. (c) Spheroid Solidity plotted as a heatmap before drug treatment (day 3 after seeding), at the day of treatment (day 4), 1 day post-treatment (day 5), and 3 days post-treatment (day 7), captured live (Cytation C10) and fixed/quenched and stained (Cytation C10 and CellInsight CX7 LZR platform). The colour indicates Z-scores compared to vehicle controls per time-point. Z-scores below  $-2$  and above  $+2$  correspond to a significant change compared to control (dashed lines). (d) Pearson correlation of day 7 live versus fixed well average Area Solidity feature ( $R^2 = 0.6655$ ).

These Area features are independent of any one channel, but Intensity and Texture features are extracted from a specific stain. In our final feature set, the different channels were represented as follows: 14 features extracted from BF channel, 12 from DAPI, three from Rhodamine Phalloidin, three from Alexa Fluor 594-WGA, and five from MTDR dye.

### 3.4.3. Active Compound Clustering

We selected active compounds based on their Mahalanobis distance, which ranged from 0.04 to 26.4. If a compound made the cut-off ( $M\text{-distance} \geq 1$ ) in any of the five concentrations, it was considered to be active. The seven compounds that did not get selected were TAK-733, AZ628, TAK-632, dabrafenib, PLX7904, sorafenib, and oxaliplatin.

Hierarchical clustering of the 48 active compounds revealed large clusters of MEK and Raf inhibitors (Figure 6b). This was an accurate reflection of the slightly unbalanced library composition, which consisted of a large number of MEK inhibitors (23 compounds; Supplementary Table S1). Reassuringly, we identified tight clustering of NF $\kappa$ B inhibitors, mTOR inhibitors, cell cycle inhibitors, and different mechanisms of DNA damage (Figure 6b).



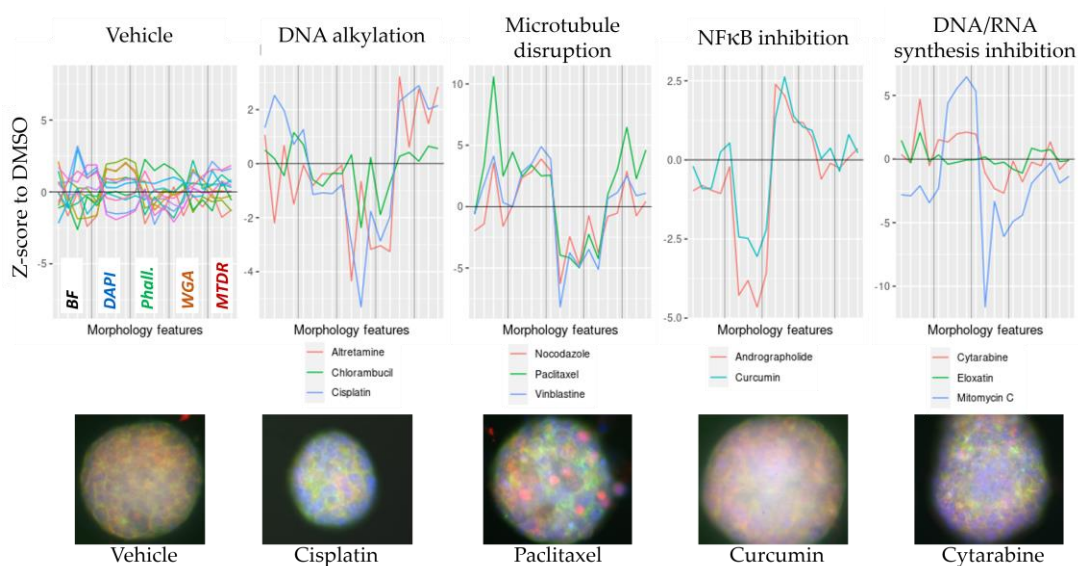
**Figure 6.** (a) Concatenated feature vector used for clustering consists of five drug concentrations with the same 150 features each. (b) Hierarchical clustering of 48 active compounds.

However, some mechanisms of action did not cluster in an obvious way, such as the EGFR inhibitors (erlotinib and gefitinib). A plausible explanation is that they may not have caused a morphological change sufficiently distinct from the MAPK inhibitors. There was also mixed success with clustering of the HMG-CoA reductase inhibitors. While lovastatin

and mevastatin appeared in the same cluster, the two other members of the MOA group, fluvastatin and simvastatin were located in other MOA clusters.

To have a closer look at the different phenotypic profiles of the various mechanisms of action in our library, we hand-selected the same representative features across all five channels to generate focused profile graphs (Figure 7):

1. Median\_Nuclei\_Intensity\_IntegratedIntensity,
2. Median\_Nuclei\_RadialDistribution\_FracAtD\_2of4,
3. Median\_Nuclei\_Texture\_InfoMeas1\_10\_00\_256 (measure of the total amount of information contained within a region of pixels derived from the recurring spatial relationship between specific intensity values),
4. StDev\_Nuclei\_Intensity\_IntegratedIntensity



**Figure 7.** Compound phenotypic profiles using four selected intensity-based features (Median Nuclei Intensity, Median Nuclei Fraction at Distance 2, Median Nuclei Texture, and Standard Deviation of Nuclei Intensity) across all five channels (Brightfield, DAPI, Rhodamine Phalloidin, Alexa Fluor 594 WGA, and MTDR dye indicated by grey vertical lines). Example composite images ( $20\times$ , one z-slice, CellInsight CX7 LZR platform) of compounds corresponding to the profiles above.

A selection of 14 vehicle-treated wells show that the negative controls have no obvious pattern in their profiles. In contrast, drugs disrupting microtubules show a clear change in texture and radial distribution features across all channels (Figure 7, Panel 3). NF $\kappa$ B-inhibitors showed no significant z-score changes in BF, Alexa Fluor 594-WGA, and MTDR channels, but caused a significant decrease in DAPI intensity features (Figure 7, Panel 4).

Interestingly, DNA alkylating agents did not significantly alter the DAPI-based features but showed a significant effect in the Rhodamine Phalloidin, Alexa Fluor 594 -WGA, and MTDR images (Figure 7, Panel 2). Composite images of a representative spheroid from some of the different mechanistic classes showed quite distinct and differentiating staining patterns.

#### 4. Discussion

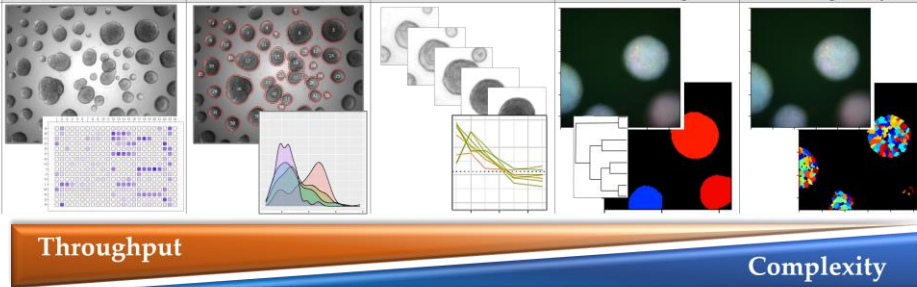
Thanks to significant advances in cell labeling, detection, and image analysis technologies, microscopy-based high-content screening is now an integral part of many high-throughput platforms to profile 2D cell models. The phenotypic screening of drug libraries or other perturbations has been successfully implemented in drug discovery and functional genomics research [1,18,19]. However, converting well-established 2D imaging pipelines into 3D methodologies to profile spheroids and organoids, while keeping them at scale and

balance sample preparation and throughput with physiological relevance, is an ongoing biological, technical, and computational challenge [2,20,21].

With the protocols outlined in this publication, we aimed to contribute to the development of high-content and high-throughput imaging methods in physiologically relevant 3D models (Figure 8). We are proposing a workflow that is:

- flexible in the cell type that can be used and depth of information that can be extracted, ranging from basic live-cell readouts to single-cell intra-organoid heterogeneity;
- economical in the use of consumables (Matrigel), patient/cell material, and imaging time;
- instrument agnostic in the required screening equipment (liquid-handling, microscope platform) as well as a publicly available image analysis software.

	Basic screening	Population heterogeneity	Time course tracking	Phenotypic profiling	Intra-organoid heterogeneity
Magnification	2×/ 4×	2×/ 4×	2×/ 4×	20×	20×/ 40×
No. of fields	1	1	1	min of 4	min of 10
No. of z-slices	1	1	1	1	1
No. of channels	1 (BF)	1 (BF)	1 (BF)	BF + 5 FL	BF + 5 FL
No. of time pt	1	1	1 to 10	1	1
Live/ fixed	Live/ fixed	Live/ fixed	Live	Fixed	Fixed
Single organoids	No	Yes	Yes	Yes	Yes
Single cells	No	No	No	No	Yes
Use for	Label-free screening using well-level BF imaging	Label-free screening using population-level data on heterogeneity	Label-free screening using time-course tracking of population	Multiplexed fixed cell staining for well-based phenotypic clustering	Single-cell analysis with targeted marker dyes for intra-organoid heterogeneity



**Figure 8.** Overview of the range of interconnected methods across the spectrum of throughput and complexity and detail.

#### 4.1. Flexible

Using our automated Matrigel seeding method [8] and the here described fixation, quenching, and staining protocols allowed us to conduct 3D imaging along various levels of throughput and complexity (Figure 8). So far, we have successfully imaged and analyzed spheroids made from cell lines (such as MCF7 breast and MR49F prostate cancer cells), patient-derived pancreatic cancer organoids (not yet published), PDX-derived prostate cancer organoids [8], esophageal adenocarcinoma patient-derived organoids [22], and colorectal cancer patient-derived tumor organoids [23].

Annotating organoid states and their plasticity upon drug treatment has been proposed to further accelerate image-based drug discovery for complex multigenic diseases such as colorectal cancer [24]. However, to capture the fluid states of 3D objects within their population, a very flexible acquisition protocol is required. In our method, the direct connection and integration of data from each organoid during its live-cell and fixed cell imaging state is only possible due to a very gentle fixation protocol. Standard FA fixation dissolves the Matrigel and neither maintains the exact location of the structures in the well, nor protects the exact morphology of the organoid in its embedded state. Therefore, many groups only use FA fixation in the context of histopathological evaluations of their

organoids in a mounted, very low-throughput way [25]. Higher throughput methods with FA-based fixation often use U-bottom plates with one single organoid in media, which lacks both population data as well as ECM interaction [11]. The alternative fixative glutaraldehyde has been reported to affect protein conformation and therefore potentially make antibody staining more challenging [26]. We have used a range of antibodies with both nuclear and cell membrane targets and successfully stained 3D cells for IF (data not shown). However, like in any staining situation, every new antibody will have to be tested first and there is a possibility that some might fail.

In the protocol proposed here, we are imaging whole wells with often more than 100 organoids during their active growth, over the whole course of genetic or pharmacological perturbation and additionally in a final fixed and stained state. This allowed us to gain unique insight into the morphological heterogeneity within each patient-derived organoid [8]. A direct extension of this application is to explore phenotypic changes between normal and cancer cell states as well as intra-organoid, cell-type specific differences through alterations in morphology, and response to treatment.

#### 4.2. Economical

These days, funding for lab research is increasingly difficult to obtain, labware and reagents are increasingly expensive, and cell material can be very rare and precious, especially patient-derived organoid samples. Therefore, we developed our protocols with their associated costs and potentially low availability in mind, using off-the-shelf, affordable chemicals and reagents for fixation, quenching, and staining. Automated seeding of cell suspension in 384-well plates requires only minimal amounts of Matrigel and cell counts per condition/well. Additionally, due to the gentle fixation process, time-course experiments and following fixed-cell analyses can be multiplexed in the same well. Currently, we are working on further multiplexing the available readouts that can be obtained from a single well by optimising MACseq [27], a miniaturized high-throughput transcriptome profiling method for Matrigel-embedded 3D spheroids and organoids.

Many 3D high-content imaging methods using confocal microscopy capture large z-stacks, ranging from 12 slices [28], to 16 slices [24], all the way to 18 z-slices [29]. Imaging to this depth would make sense if the 3D objects were being analyzed in true 3D mode (voxels instead of pixels), as it has been shown that unsupervised voxel-based feature learning yields much better clustering results of drug-treatment related morphological changes compared to 2D pixel-based image analysis [29]. However, this type of analysis requires a level of computational effort that is too extensive for most high-throughput screening projects and the majority of groups end up using only one final image per field in 2D analysis mode after maximum contrast projection of their large z-stacks [24,28]. To achieve the development of a true high-throughput method, we aimed to decrease the required scanning time per plate to the absolute minimum without compromising the data quality. Our analyses showed that the data extracted from the different z-slices were on average 95% identical (Figure 4c), and therefore, we propose to acquire only a single z-slice for further analysis. It was very encouraging to see that even with just a single z-slice and a very generic, non-targeted staining panel, we were able to extract imaging profiles that were compound specific enough to cluster by their mechanism of action (Figure 7).

#### 4.3. Instrument Agnostic

The final goal we wanted to achieve with the workflows presented here was to democratize high-content and high-throughput screening in complex 3D models, so that it becomes easier accessible even to smaller labs or facilities without a large budget. All liquid handling required for fixation, quenching, and staining can be performed on BioTek EL406 liquid handling workstations. While we used the Perkin Elmer Janus for seeding of Matrigel-cell suspensions and transfer of compound libraries, there are multiple liquid handling options available, that would be adequate substitutes [30,31]. Additionally, all our live-cell methods on image acquisition, spheroid segmentation based on brightfield,



and downstream image and data analyses are also applicable in 3D structures seeded in hydrogels with bioprinters such as the RASTRUM bioprinter [32]. Finally, we made sure that all imaging magnifications ( $2\times$ ,  $10\times$ ,  $20\times$ ) and the concentrations of our proposed staining panel work both on the Cytation suite of imagers (5 and C10) as well as on the CellInsight CX7 platforms (LED and LZR).

In summary, this study presents effective guidelines for sample preparation, labeling, and high content image analysis applicable to the wide range of spheroid- and organoid-based models being utilized in biological research as well as drug discovery and development. Considerations and data presented here provide a framework within which additional probes should be evaluated in various combinations to define useful panels of targets with multiplex labeling and image analysis protocols to expand information available in organoid/spheroid- and cell-level screening.

**Supplementary Materials:** The following supporting information can be downloaded at: <https://www.mdpi.com/article/10.3390/organoids2010001/s1>, Table S1: Mechanism of Action compound library. Table S2: Summary of features for image clustering. Figure S1: Dilution series of FA from 4% to 0.01% and effect on the Matrigel after incubation for 10 min at RT. If the imaging height is kept the same as the pre-fix acquisition, all MCF7 spheroids are out of focus due to the loss of supporting matrix (both 2% embedding Matrigel and 80% base layer). Spheroids are back in focus if the focal plane is changed to the bottom of the well. Furthermore, the relative position of structures in every one of these fixation settings has completely changed.

**Author Contributions:** Conceptualization, S.R. and K.J.S.; methodology, R.V., J.L., K.J.C., M.S.J., N.R. and T.G.; software, S.R. and K.J.C.; formal analysis, S.R.; resources, R.V., J.L., K.J.C., M.S.J., N.R. and K.J.S.; data curation, S.R. and R.V.; writing—original draft preparation, S.R. and T.G.; writing—review and editing, S.R. and K.J.S.; visualization, R.V., J.L., K.J.C. and S.R.; supervision, K.J.S.; project administration, K.J.S.; funding acquisition, K.J.S. All authors have read and agreed to the published version of the manuscript.

**Funding:** The Victorian Centre for Functional Genomics (K.J.S.) is funded by the Australian Cancer Research Foundation (ACRF), Phenomics Australia (PA) through funding from the Australian Government's National Collaborative Research Infrastructure Strategy (NCRIS) program, the Peter MacCallum Cancer Centre Foundation, and the University of Melbourne Research Collaborative Infrastructure Program (MCRIP).

**Institutional Review Board Statement:** The studies were conducted in accordance with the National Statement on Ethical Conduct in Human Research produced by the National Health and Medical Research Council of Australia. All animal handling and procedures used to establish and maintain the PDXs were approved by the Monash University Standing Committee of Ethics in Animal Experimentation (MARP 2012/158, MARP/2014/085, MARP 28911).

**Informed Consent Statement:** Patient-derived xenografts were established by the Melbourne Urological Research Alliance (MURAL) with informed written consent according to human ethics approvals from Peter MacCallum Cancer Centre (11/102), Cabrini Health (03-14-04-08) and Monash University (1636, 12287).

**Data Availability Statement:** Not applicable.

**Acknowledgments:** We thank the Centre for Advanced Histology and Microscopy (CAHM) at the Peter MacCallum Cancer Centre, Victoria, Australia for the provision of glutaraldehyde. We thank Guillaume Morin, Support Manager Australasia at Thermo Fisher Scientific, for ongoing instrument support and his facilitation in reagent procurement. We thank Renea A. Taylor, Mitchell G. Lawrence, and Gail P. Risbridger from Monash Biomedicine Discovery Institute Cancer Program, Prostate Cancer Research Group, Monash University, Clayton, VIC, Australia, who are part of the Melbourne Urological Research Alliance (MURAL) for provision of prostate cancer cell lines and patient-derived prostate cancer organoids.

**Conflicts of Interest:** The authors from the Peter MacCallum Cancer Centre declare no conflict of interest. Nicholas Radio is a global product manager for high-content technologies at Thermo Fisher Scientific. Michael Janes is a research and development scientist at Thermo Fisher Scientific.

## References

1. Carpenter, A.E. Image-based chemical screening. *Nat. Chem. Biol.* **2007**, *3*, 461–465. [[CrossRef](#)] [[PubMed](#)]
2. Lukonin, I.; Zinner, M.; Liberali, P. Organoids in image-based phenotypic chemical screens. *Exp. Mol. Med.* **2021**, *53*, 1495–1502. [[CrossRef](#)] [[PubMed](#)]
3. Birgersdotter, A.; Sandberg, R.; Ernberg, I. Gene expression perturbation in vitro—A growing case for three-dimensional (3D) culture systems. *Semin. Cancer Biol.* **2005**, *15*, 405–412. [[CrossRef](#)] [[PubMed](#)]
4. Edmondson, R.; Broglie, J.J.; Adcock, A.F.; Yang, L. Three-dimensional cell culture systems and their applications in drug discovery and cell-based biosensors. *Assay Drug Dev. Technol.* **2014**, *12*, 207–218. [[CrossRef](#)] [[PubMed](#)]
5. Proctor, W.R.; Foster, A.J.; Vogt, J.; Summers, C.; Middleton, B.; Pilling, M.A.; Shienson, D.; Kijanska, M.; Strobel, S.; Kelm, J.M.; et al. Utility of spherical human liver microtissues for prediction of clinical drug-induced liver injury. *Arch. Toxicol.* **2017**, *91*, 2849–2863. [[CrossRef](#)]
6. Kenny, H.A.; Lal-Nag, M.; White, E.A.; Shen, M.; Chiang, C.Y.; Mitra, A.K.; Zhang, Y.; Curtis, M.; Schryver, E.M.; Bettis, S.; et al. Quantitative high throughput screening using a primary human three-dimensional organotypic culture predicts in vivo efficacy. *Nat. Commun.* **2015**, *6*, 6220. [[CrossRef](#)]
7. Beghin, A.; Greci, G.; Sahni, G.; Guo, S.; Rajendiran, H.; Delaire, T.; Mohamad Raffi, S.B.; Blanc, D.; de Mets, R.; Ong, H.T.; et al. Automated high-speed 3D imaging of organoid cultures with multi-scale phenotypic quantification. *Nat. Methods* **2022**, *19*, 881–892. [[CrossRef](#)]
8. Choo, N.; Ramm, S.; Luu, J.; Winter, J.M.; Selth, L.A.; Dwyer, A.R.; Frydenberg, M.; Grummet, J.; Sandhu, S.; Hickey, T.E.; et al. High-Throughput Imaging Assay for Drug Screening of 3D Prostate Cancer Organoids. *SLAS Discov.* **2021**, *26*, 1107–1124. [[CrossRef](#)]
9. Bray, M.A.; Singh, S.; Han, H.; Davis, C.T.; Borgeson, B.; Hartland, C.; Kost-Alimova, M.; Gustafsdottir, S.M.; Gibson, C.C.; Carpenter, A.E. Cell Painting, a high-content image-based assay for morphological profiling using multiplexed fluorescent dyes. *Nat. Protoc.* **2016**, *11*, 1757–1774. [[CrossRef](#)]
10. Broguiere, N.; Isenmann, L.; Hirt, C.; Ringel, T.; Placzek, S.; Cavalli, E.; Ringnalda, F.; Villiger, L.; Züllig, R.; Lehmann, R.; et al. Growth of Epithelial Organoids in a Defined Hydrogel. *Adv. Mater.* **2018**, *30*, 1801621. [[CrossRef](#)]
11. Boutin, M.E.; Voss, T.C.; Titus, S.A.; Cruz-Gutierrez, K.; Michael, S.; Ferrer, M. A high-throughput imaging and nuclear segmentation analysis protocol for cleared 3D culture models. *Sci. Rep.* **2018**, *8*, 11135. [[CrossRef](#)] [[PubMed](#)]
12. Rezakhani, S.; Gjorevski, N.; Lutolf, M.P. Extracellular matrix requirements for gastrointestinal organoid cultures. *Biomaterials* **2021**, *276*, 121020. [[CrossRef](#)] [[PubMed](#)]
13. Heo, J.H.; Kang, D.; Seo, S.J.; Jin, Y. Engineering the Extracellular Matrix for Organoid Culture. *Int. J. Stem Cells* **2022**, *15*, 60–69. [[CrossRef](#)] [[PubMed](#)]
14. Risbridger, G.P.; Clark, A.K.; Porter, L.H.; Toivanen, R.; Bakshi, A.; Lister, N.L.; Pook, D.; Pezaro, C.J.; Sandhu, S.; Keerthikumar, S.; et al. The MURAL collection of prostate cancer patient-derived xenografts enables discovery through preclinical models of uro-oncology. *Nat. Commun.* **2021**, *12*, 5049. [[CrossRef](#)]
15. Hutz, J.E.; Nelson, T.; Wu, H.; McAllister, G.; Moutsatsos, I.; Jaeger, S.A.; Bandyopadhyay, S.; Nigsch, F.; Cornett, B.; Jenkins, J.L.; et al. The Multidimensional Perturbation Value: A Single Metric to Measure Similarity and Activity of Treatments in High-Throughput Multidimensional Screens. *J. Biomol. Screen.* **2012**, *18*, 367–377. [[CrossRef](#)]
16. Clancy, B.; Cauller, L.J. Reduction of background autofluorescence in brain sections following immersion in sodium borohydride. *J. Neurosci. Methods* **1998**, *83*, 97–102. [[CrossRef](#)]
17. Boland, M.V.; Markey, M.K.; Murphy, R.F. Automated recognition of patterns characteristic of subcellular structures in fluorescence microscopy images. *Cytometry* **1998**, *33*, 366–375. [[CrossRef](#)]
18. Boutros, M.; Heigwer, F.; Laufer, C. Microscopy-Based High-Content Screening. *Cell* **2015**, *163*, 1314–1325. [[CrossRef](#)]
19. Pegoraro, G.; Misteli, T. High-Throughput Imaging for the Discovery of Cellular Mechanisms of Disease. *Trends Genet.* **2017**, *33*, 604–615. [[CrossRef](#)]
20. Badder, L.M.; Hollins, A.J.; Herpers, B.; Yan, K.; Ewan, K.B.; Thomas, M.; Shone, J.R.; Badder, D.A.; Naven, M.; Ashelford, K.E.; et al. 3D imaging of colorectal cancer organoids identifies responses to Tankyrase inhibitors. *PLoS ONE* **2020**, *15*, e0235319. [[CrossRef](#)]
21. Bock, C.; Boutros, M.; Camp, J.G.; Clarke, L.; Clevers, H.; Knoblich, J.A.; Liberali, P.; Regev, A.; Rios, A.C.; Stegle, O.; et al. The Organoid Cell Atlas. *Nat. Biotechnol.* **2021**, *39*, 13–17. [[CrossRef](#)] [[PubMed](#)]
22. Ceder, S.; Eriksson, S.E.; Cheteh, E.H.; Dawar, S.; Corrales Benitez, M.; Bykov, V.J.N.; Fujihara, K.M.; Grandin, M.; Li, X.; Ramm, S.; et al. A thiol-bound drug reservoir enhances APR-246-induced mutant p53 tumor cell death. *EMBO Mol. Med.* **2021**, *13*, e10852. [[CrossRef](#)] [[PubMed](#)]
23. Behrenbruch, C.; Foroutan, M.; Lind, P.; Smith, J.; Grandin, M.; Cooper, B.; Shembrey, C.; Ramm, S.; Cowley, K.; Nikolic, I.; et al. Targeting of TP53-independent cell cycle checkpoints overcomes FOLFOX resistance in Metastatic Colorectal Cancer. *bioRxiv* **2021**. [[CrossRef](#)]
24. Betge, J.; Rindtorff, N.; Sauer, J.; Rauscher, B.; Dingert, C.; Gaitantzi, H.; Herweck, F.; Srour-Mhanna, K.; Miersch, T.; Valentini, E.; et al. The drug-induced phenotypic landscape of colorectal cancer organoids. *Nat. Commun.* **2022**, *13*, 3135. [[CrossRef](#)] [[PubMed](#)]
25. Fujii, E.; Yamazaki, M.; Kawai, S.; Ohtani, Y.; Watanabe, T.; Kato, A.; Suzuki, M. A simple method for histopathological evaluation of organoids. *J. Toxicol. Pathol.* **2018**, *31*, 81–85. [[CrossRef](#)] [[PubMed](#)]

26. McKenzie, A.T. Glutaraldehyde: A Review of Its Fixative Effects on Nucleic Acids, Proteins, Lipids, and Carbohydrates. [[CrossRef](#)]
27. Kong, I.Y.; Trezise, S.; Light, A.; Todorovski, I.; Arnau, G.M.; Gadipally, S.; Yoannidis, D.; Simpson, K.J.; Dong, X.; Whitehead, L.; et al. Epigenetic modulators of B cell fate identified through coupled phenotype-transcriptome analysis. *Cell Death Differ.* **2022**, *29*, 2519–2530. [[CrossRef](#)]
28. Lukonin, I.; Serra, D.; Challet Meylan, L.; Volkmann, K.; Baaten, J.; Zhao, R.; Meeusen, S.; Colman, K.; Maurer, F.; Stadler, M.B.; et al. Phenotypic landscape of intestinal organoid regeneration. *Nature* **2020**, *586*, 275–280. [[CrossRef](#)]
29. Mergenthaler, P.; Hariharan, S.; Pemberton, J.M.; Lourenco, C.; Penn, L.Z.; Andrews, D.W. Rapid 3D phenotypic analysis of neurons and organoids using data-driven cell segmentation-free machine learning. *PLoS Comput. Biol.* **2021**, *17*, e1008630. [[CrossRef](#)]
30. Hongisto, V.; Jernstrom, S.; Fey, V.; Mpindi, J.P.; Kleivi Sahlberg, K.; Kallioniemi, O.; Perala, M. High-throughput 3D screening reveals differences in drug sensitivities between culture models of JIMT1 breast cancer cells. *PLoS ONE* **2013**, *8*, e77232. [[CrossRef](#)]
31. Du, Y.; Li, X.; Niu, Q.; Mo, X.; Qui, M.; Ma, T.; Kuo, C.J.; Fu, H. Development of a miniaturized 3D organoid culture platform for ultra-high-throughput screening. *J. Mol. Cell Biol.* **2020**, *12*, 630–643. [[CrossRef](#)]
32. Engel, M.; Belfiore, L.; Aghaei, B.; Sutija, M. Enabling high throughput drug discovery in 3D cell cultures through a novel bioprinting workflow. *SLAS Technol.* **2022**, *27*, 32–38. [[CrossRef](#)] [[PubMed](#)]

**Disclaimer/Publisher’s Note:** The statements, opinions and data contained in all publications are solely those of the individual author(s) and contributor(s) and not of MDPI and/or the editor(s). MDPI and/or the editor(s) disclaim responsibility for any injury to people or property resulting from any ideas, methods, instructions or products referred to in the content.